

**O₂ Emission Toward Orion H₂ Peak 1
and the Role of FUV-Illuminated C-Shocks**

Gary Melnick¹ and Michael J. Kaufman²,

To appear in the Astrophysical Journal

Received Feb. 19, 2015 ; Accepted May 4, 2015

¹ Harvard-Smithsonian Center for Astrophysics, 60 Garden Street, MS 66, Cambridge, MA 02138, USA

² Department of Physics and Astronomy, San José State University, San José, CA 95192, USA

ABSTRACT

Molecular oxygen (O_2) has been the target of ground-based and space-borne searches for decades. Of the thousands of lines of sight surveyed, only those toward Rho Ophiuchus and Orion H_2 Peak 1 have yielded detections of any statistical significance. The detection of the O_2 $N_J = 3_3 - 1_2$ and $5_4 - 3_4$ lines at 487.249 GHz and 773.840 GHz, respectively, toward Rho Ophiuchus has been attributed to a short-lived peak in the time-dependent, cold-cloud O_2 abundance, while the detection of the O_2 $N_J = 3_3 - 1_2$, $5_4 - 3_4$ lines, plus the $7_6 - 5_6$ line at 1120.715 GHz, toward Orion has been ascribed to time-dependent preshock physical and chemical evolution and low-velocity (12 km s^{-1}) non-dissociative C -type shocks, both of which are fully shielded from far-ultraviolet (FUV) radiation, plus a postshock region that is exposed to a FUV field. We report a re-interpretation of the Orion O_2 detection based on new C -type shock models that fully incorporate the significant effects the presence of even a weak FUV field can have on the preshock gas, shock structure and postshock chemistry. In particular, we show that a family of solutions exists, depending on the FUV intensity, that reproduces *both* the observed O_2 intensities and O_2 line ratios. The solution in closest agreement with the shock parameters inferred for H_2 Peak 1 from other gas tracers assumes a 23 km s^{-1} shock impacting gas with a preshock density of $8 \times 10^4 \text{ cm}^{-3}$ and $G_o = 1$, substantially different from that inferred for the fully-shielded shock case. As pointed out previously, the similarity between the LSR velocity of all three O_2 lines ($\approx 11 \text{ km s}^{-1}$) and recently measured H_2O $5_{32} - 4_{41}$ maser emission at 620.701 GHz toward H_2 Peak 1 suggests that the O_2 emission arises behind the same shocks responsible for the maser emission, though the O_2 emission is almost certainly more extended than the localized high-density maser spots. Since maser emission arises along lines of sight of low-velocity gradient, indicating shock motion largely perpendicular to our line of sight, we note that this geometry can not only explain the narrow ($\lesssim 3 \text{ km s}^{-1}$) observed O_2 line widths despite their excitation behind a shock, but also why such O_2 detections are rare.

Subject headings: astrochemistry – ISM: abundances – ISM: individual objects (Orion) – ISM: molecules – submillimeter: ISM

1. INTRODUCTION

Accounting for the low abundance of molecular oxygen (O_2) in dense ($n(\text{H}_2) \gtrsim 10^3 \text{ cm}^{-3}$) molecular clouds has long posed a challenge to both observers and theorists. For almost 30 years, the search for O_2 was motivated by predictions of gas-phase chemical models that O_2 was a major reservoir of elemental oxygen within dense clouds (e.g. Goldsmith & Langer 1978; Neufeld, Lepp & Melnick 1995). However, the inability of gas-phase models to account for the observed abundance of an increasing number of species highlighted the shortcomings of such models. This became evident again following the launch of the *Submillimeter Wave Astronomy Satellite (SWAS)* (Melnick et al. 2000) and *Odin* (Nordh et al. 2003) when their largely unsuccessful searches for O_2 established upper limits to the O_2 abundance more than 100 times below the predictions of these models (e.g., Goldsmith et al. 2000). Modified chemical models, which include the effects of dust grains as sites for molecule formation as well as freeze out, were then invoked to explain the low O_2 abundance and weak emission (cf. Bergin et al. 2000; Hollenbach et al. 2009). With the launch of the *Herschel Space Observatory* (Pilbratt et al. 2010), attention turned to using its greater sensitivity to target regions predicted by these updated chemical models to possess high columns of warm O_2 .

The Open Time Key Program, *Herschel* Oxygen Project (HOP), was proposed and selected to carry out a survey of warm molecular clouds in the following rotational transitions of O_2 : $(N, J) = (3,3) \rightarrow (1,2)$ at 487 GHz, $(5,4) \rightarrow (3,4)$ at 774 GHz, and $(7,6) \rightarrow (5,6)$ at 1121 GHz (see Goldsmith et al. 2011). Among the sources of particular interest was the Orion Molecular Cloud because of the large column densities of warm molecular gas known to exist toward several prominent components, including the Hot Core, the Orion Bar, and H_2 Peaks 1 and 2. While no convincing O_2 emission was detected toward the Hot Core (Goldsmith et al. 2011) or Orion Bar (Melnick et al. 2012), O_2 emission has been detected toward H_2 Peak 1 (Goldsmith et al. 2011; Chen et al. 2014). This detection raises two questions: (1) What plausible conditions exist at H_2

Peak 1 that could produce the observed O₂ line intensities *and* line ratios?; and, (2) Are these conditions nonetheless sufficiently rare to explain the absence of detectable O₂ emission toward most other sources searched?

Intense H₂ emission toward Peak 1 is observed in transitions with excitation energies, E_u/k , ranging from 1015 to 43,000 K that has long been attributed to collisional excitations due to shock waves presumed to result from the high-velocity outflow originating $\sim 30''$ to the SE in the BN/KL region (Gautier et al. 1976; Beckwith et al. 1978; Rosenthal, Bertoldi & Drapatz 2000). The Orion Molecular Cloud is also subject to strong far-ultraviolet (FUV) radiation from sources such as θ^1 C Ori (cf. Kristensen et al. 2003). In this paper, we examine the role FUV radiation plays in altering the chemical and physical conditions in gas capable of reproducing the O₂ observations reported in Chen et al. (2014). In particular, we focus on FUV-illuminated gas subject to the passage of non-dissociative *C*-type shocks as regions especially conducive to the production of elevated O₂ abundances.

Fully shielded non-dissociative shocks are generally inefficient at producing O₂ in the post-shocked gas. Even when shock velocities are sufficient to sputter material from grain surfaces, all but $\sim 1\%$ of the gas-phase oxygen not locked in CO is rapidly processed into H₂O within the warm ($T \gtrsim 400$ K) postshock gas via a set of neutral-neutral chemical reactions ($\text{O} + \text{H}_2 \rightarrow \text{OH} + \text{H}$; $\text{OH} + \text{H}_2 \rightarrow \text{H}_2\text{O} + \text{H}$). In the absence of a FUV field, the H₂O abundance is predicted to remain high throughout the postshock region and the O₂ abundance never exceeds a few percent of that of H₂O (cf. Draine et al. 1983; Kaufman & Neufeld 1996b). However, the presence of a FUV field can significantly increase the postshock O₂ abundance by: (1) increasing the preshock atomic oxygen abundance through both the photodissociation of gas-phase O-bearing species and the photodesorption (from grains) and subsequent photodissociation of desorbed O-bearing species, leading to a higher postshock H₂O abundance; and, (2) increasing the postshock abundance of OH and O through the photodissociation of postshock H₂O,

enabling increased production of O_2 via the reaction $O+OH \rightarrow O_2+H$.

In Chen et al. (2014), the three components necessary to model the observed O_2 emission – i.e., the preshock gas, the shock and its postshock thermal profile, and the postshock chemistry – were addressed separately. In particular, the preshock gas and shock were assumed to be fully shielded, i.e., no FUV radiation reaches these regions, while the postshock chemistry was modeled assuming various levels of FUV illumination. It is unlikely that the preshock, shock, and postshock gas, which are in close physical proximity, would experience significantly different FUV fluxes; however, the absence of a shock code that incorporates the full effects of a FUV field dictated the approach described in Chen et al.

In this paper, we re-examine the results presented in Chen et al., with several important differences. The main contribution of the present work is the self-consistent treatment of the preshock, shock, and postshock regions under the influence of FUV fields common to all components. FUV radiation can not only increase the preshock atomic oxygen abundance, as described above, but the effects of FUV radiation on the structure of *C*-type shocks can be significant. These effects include increased postshock temperatures at a given shock velocity, reduced velocities at which these shocks break down (and H_2 is dissociated), as well as the altered abundance of key postshock molecular species. We will show that: (1) the thermal and chemical changes induced by the FUV radiation on the preshock, shock, and postshock gas, and including the sputtering of H_2O from grain mantles at shock velocities greater than $\sim 20 \text{ km s}^{-1}$, yield multiple combinations of shock velocity and FUV field intensity capable of producing detectable O_2 emission; and, (2) the O_2 line intensity ratios can be an important discriminator between shock models. Use of the observed O_2 line ratios was not used as a test of the shock models presented in Chen et al.

In addition, the inclusion of a FUV field in all gas components mitigates a problem identified in Chen et al., i.e., the need in their model to assume $\gtrsim 10\%$ sputtering efficiency of H_2O from

grain mantles behind a 12 km s^{-1} *C*-type shock. As will be discussed, a sputtering efficiency of 10% or greater behind a 12 km s^{-1} shock is higher than theoretical predictions as well as recent observations.

Finally, the association between co-located H_2O maser emission and the O_2 emission noted in Chen et al. provides important clues regarding the orientation of the H_2O - and likely the O_2 -producing shocks. We point out that this orientation not only justifies the assumption of relatively large column densities of O_2 along the line of sight, as discussed in Chen et al., but also provides an alternate explanation to that offered in Chen et al. for why such O_2 detections are rare.

In §2, we briefly review the O_2 observations upon which our analysis is based. In §3, we describe the modifications to the *C*-type shock models required when such shocks are exposed to FUV radiation. In §4, we describe the assumed shock geometry, the methods used to compute the O_2 line integrated intensities, and how well the results fit the observations. In §5, we discuss the ways in which FUV-illuminated *C*-type shocks and the shock geometry toward Orion H_2 Peak 1 combine to provide an explanation for the detected O_2 emission while also accounting for the apparent rarity of such emission.

2. OBSERVATIONS AND RESULTS

The *Herschel* observational results considered in this paper are presented in Chen et al. (2014). The interested reader is referred to Chen et al. for details regarding the observations and data reduction; only the results we model are summarized here.

The observations were conducted in 2012 using the Heterodyne Instrument for the Far Infrared (HIFI; de Graauw et al. 2010) and were centered at J2000 coordinates $\text{R.A.} = 5^{\text{h}} 35^{\text{m}} 14.^{\text{s}}2$ and $\text{Dec.} = -5^{\circ} 22' 31''$. HIFI was used in dual beam switch (DBS) mode with the reference po-

sitions located 3' on either side of the source. For each transition, eight local oscillator (LO) settings were used to allow sideband deconvolution. The integration time for each LO setting was 824 seconds for the 487 GHz and 774 GHz spectra, and 3477 seconds for the 1121 GHz spectrum. The observational results relevant to our modeling effort are presented in Table 1.

3. MODIFIED SHOCK MODELS

3.1. *FUV-Illuminated C-Type Shocks*

Within interstellar shocks possessing low fractional ionization and a strong magnetic field, the flow variables may remain continuous; i.e., the neutral and ionized gases do not experience discontinuities and the gas remains relatively cool and molecular. The physics of *C*-type shocks in well-shielded gas has been studied extensively (e.g., Draine 1983; Draine et al. 1983; Kaufman & Neufeld 1996a; Flower & Pineau des Florêts 2010); however, it is increasingly evident that FUV radiation from nearby stars plays a role in the physics of molecular outflows (e.g., Kristensen et al. 2012; van Kempen et al. 2010). In order to assess the role of FUV radiation, we have made several modifications to the Kaufman & Neufeld (1996a) model. These modifications affect the abundances of important species in the preshock gas, the shock length scale, and the abundances of oxygen-bearing species in the postshock gas. We briefly describe the effects below; a more detailed description will be included in a forthcoming paper.

3.2. *Preshock Conditions*

To determine the conditions in the preshock molecular gas, we use the detailed photodissociation region (PDR) model of Hollenbach et al. (2009). This model computes the abundances of numerous atomic and molecular species, as well as those of charged and neutral dust grains and PAHs, as a function of extinction into a cloud, given the input parameters of gas density, n , and FUV radiation field strength, G_o (scaling factor in multiples of the average Habing local

interstellar radiation field; Habing 1968). In order to model a shock propagating through such gas, the important outputs of the PDR model are: (i) the types and abundances of charge carriers, which determine how well the ionized species couple to the magnetic field; and (ii) the abundances of gas-phase species, especially oxygen- and carbon-bearing species that become incorporated into important gas coolants. It is the interplay between momentum transfer (moderated by the coupling length) and the efficiency of gas cooling (which limits the gas temperature) that determines the final shock structure. As shown by Hollenbach et al. (2009), significant fractions of oxygen and carbon nuclei can be locked up on the surfaces of dust grains in molecular gas exposed to moderate FUV fields at extinctions $A_V \sim 1$. Based on the same PDR model described in detail in Hollenbach et al. (2009), Fig. 1 shows the preshock gas-phase abundances of H_2O and O as functions of density and G_o .

To first order, the length scale depends only on the ionization fraction and the strength of the magnetic field. In gas fully-shielded from FUV radiation, the fractional ionization is set by the cosmic ray ionization rate and is low, resulting in a relatively long ion-neutral coupling length scale and C -shocks that can be supported up to velocities of $\sim 40 \text{ km s}^{-1}$. In unshielded gas, the fractional ionization reaches its maximum value of $\sim 10^{-4}$, set by the carbon abundance, and results in the shortest possible length scale. In gas at $A_V = 1$, the length scale is between these two extremes and depends sensitively on the gas density and grain properties. An important point arising from these calculations is that, because the length scale is shorter than in fully-shielded gas, the maximum C -shock velocity is generally less than 40 km s^{-1} .

3.3. *Postshock Chemistry*

Within the shock, the abundances of gas-phase O-bearing species are set by competition between neutral-neutral reactions, which tend to drive O nuclei into O_2 , OH and H_2O , and photodissociation, which destroys these molecules. Studies of C -type shocks in fully-shielded gas show that

O-nuclei are efficiently driven into H₂O once the gas temperature exceeds ~ 400 K, at shock velocities $\gtrsim 10-15$ km s⁻¹; in the absence of photodissociation, the H₂O abundance remains high in the postshock gas. The presence of FUV radiation has two effects. First, it shortens the length scale and thus lowers the shock velocity at which the gas reaches 400 K. Second, it destroys molecules in the cooling postshock gas; to account for this, we have added photodissociation reactions to the shock chemical scheme, including dissociation of H₂O, OH and O₂. Under these conditions, the gas has higher abundances of O and OH than without photodissociation. The O and OH are driven into molecular oxygen by the reaction $O + OH \rightarrow O_2 + H$, which has a reaction rate that is within a factor of two of 3×10^{-11} cm³ s⁻¹ over the range 10 K to 500 K (McElroy et al. 2013). This is in contrast with the neutral-neutral reactions that drive O into OH and H₂O, each of which has barriers of > 1000 K. We find that the postshock O₂ abundance is directly correlated with the preshock gas-phase O-nuclei abundance; more O-nuclei in the preshock gas lead to more H₂O in the warm gas followed by more O₂ in the cooler gas.

In addition to increases in the preshock gas-phase O-nuclei abundance caused by FUV radiation, H₂O can be removed from ice mantles by the shocks themselves. Ice mantles on grains are sputtered by ion-neutral collisions in shocked regions where there is substantial relative velocity between charged grains and neutral molecules. We follow the treatment of Flower & Pineau des Florêts (1994) for the removal of oxygen and water-ice mantles, but with a threshold energy for ice removal consistent with that found by Neufeld et al. (2014), i.e. complete grain mantle removal for shocks with $v_s > 25$ km s⁻¹. Note that these results are similar to those found by both Draine et al. (1983) and Jiménez-Serra et al. (2008), who find $\sim 10\%$ of mantles are removed in 20 km s⁻¹ shocks. At velocities less than ~ 20 km s⁻¹, sputtering of grain mantles is not expected to be efficient, so the gas-phase abundances of O and C nuclei should be unchanged by the passage of such slower shocks.

Because the O₂ itself is subject to photodissociation, the O₂ abundance, $N(O_2)/N(H_2) = \chi(O_2)$,

does not reach the abundance of O-nuclei in the gas. An example may be seen Fig. 2 in which models with $G_o = 0.1$, 1 and $G_o = 10$ are compared. Note that the peak O_2 abundance is higher in the $G_o = 10$ case since the higher G_o keeps more O in the gas phase. Moreover, the higher postshock gas temperatures when G_o is high allow the neutral-neutral reactions to more than compensate for the photodestruction of H_2O while $T \gtrsim 300$ K, keeping the H_2O abundance high; however, when T drops below ~ 300 K, the H_2O photodestruction rate exceeds its formation rate and the H_2O abundance quickly drops, as shown in Fig. 2.

The conditions necessary to provide a significant O_2 column are: (i) a large fraction of O-nuclei in the preshock gas; (ii) sufficient FUV radiation to dissociate the shock-produced H_2O , but not so much that no significant O_2 survives in the postshock gas; and (iii) a FUV flux that remains below the threshold at which the length scale will no longer support C -shocks.

4. MODELING APPROACH

4.1. Shock Geometry

Chen et al. (2014) have identified Orion H_2 Peak 1 as the most likely source of the reported O_2 emission. Peak 1 is the site where the high-velocity gas from the dynamical center of the outflow, about $30''$ to the southeast in the vicinity of the BN/KL region, impacts the surrounding cloud, creating strong and extended collisionally-excited near-infrared H_2 emission (Cunningham 2006) as well as 22 GHz H_2O maser emission (cf. Genzel et al. 1981). Using *Herschel*/HIFI, Neufeld et al. (2013) recently reported the detection of H_2O maser emission arising from the $5_{32} - 4_{41}$ rotational transition at 620.701 GHz toward H_2 Peak 1 (see Fig. 3). As noted in Chen et al., the similarity between the LSR velocities of the maser emission of ≈ 11 km s $^{-1}$ and that of the O_2 suggests a connection.

Along with 22 GHz H_2O maser observations obtained during the same epoch, Neufeld et al. in-

interpret the maser emission as being consistent with a pumping model in which the population inversions arise from the combined effects of collisional excitation and spontaneous radiative decay. Moreover, because collisional excitations that produce a population inversion in the $5_{32} - 4_{41}$ transition require H_2 densities greater than 10^8 cm^{-3} (cf. Neufeld & Melnick 1991), and because the upper 5_{32} state lies 698 K above the ground state, gas compressed and heated behind a shock front provides the most plausible explanation for the source of this maser emission. Finally, the direction of maximum gain for stimulated emission lies along the path with the minimum velocity gradient which, for a C -type shock, is perpendicular to the direction of propagation. Thus, it's likely that the shocks giving rise to the 22 GHz and 621 GHz H_2O masers toward H_2 Peak 1 are propagating perpendicular to our line of sight. While we are not suggesting that the O_2 emission necessarily arises from the H_2O maser spots, the presence of the H_2O masers points to shocks moving in the plane of the sky, some of which achieve high enough postshock densities and temperatures to produce maser action, but most of which may not. Such a scenario has significant advantages for explaining the O_2 emission observed toward H_2 Peak 1: (1) shocks viewed in cross section (vs. face-on) can potentially present the observer with a large column of gas with a relatively high postshock O_2 abundance; and, (2) the propagation velocity of the shocks in the plane of the sky can assume any value (up to the C -type shock breakdown velocity), while the line-of-sight velocity gradient can be low, and thus consistent with the narrow ($\lesssim 3 \text{ km s}^{-1}$) O_2 line widths observed (see Table 1). This geometry is shown schematically in Fig. 4.

4.2. Shock Models and O_2 Emission

A series of shock models were generated for preshock densities ranging between 10^3 cm^{-3} and 10^6 cm^{-3} in steps of 0.1 dex and incident FUV fluxes, G_o , of 0.1, 1, and 10. For each value of G_o and preshock density, shock velocities ranging from 5 km s^{-1} up to the C -shock breakdown

velocity, in steps of 1 km s^{-1} , were also generated. In total, 839 shock models were computed for a $G_o = 0.1$, 618 models were computed for a $G_o = 1$, and 455 models were computed for a $G_o = 10$. That fewer models were generated as G_o increases reflects the fact that as G_o increases, *C*-type shocks break down at lower shock velocities. Thus, a smaller range of shock velocities – and models – are consistent with *C*-type shocks as G_o rises.

For each shock model, the postshock H_2 density, temperature, and H_2O , OH , and O_2 abundance are computed as a function of distance behind the shock front. The range of postshock distances considered extends beyond where: (1) the H_2O , OH , and O_2 abundances peak and subsequently drop by at least a factor of 10; and, (2) the postshock temperature drops to 10 K. Meeting these criteria ensures that our modeling captures essentially all of the O_2 emission since, beyond the postshock distances we consider, the reduced O_2 abundances combined with the low gas temperatures produce negligible contributions to the total O_2 integrated intensity.

Within the postshock region in which the density, temperature and O_2 abundance favor non-negligible O_2 emission (as defined above), the gas is divided into 1000 equally-spaced zones, each characterized by an H_2 density, temperature, and O_2 abundance (relative to H_2) as computed by the *C*-shock code. To obtain the O_2 line intensities from each zone, the equilibrium level populations have been calculated using an escape probability method. We use the rate coefficients for collisions between O_2 and He computed by Lique (2010), multiplied by 1.37 to account for the different reduced mass when H_2 is the collision partner. Since these rates were computed for gas temperatures $\leq 350 \text{ K}$, extrapolation to higher temperatures was necessary for application to postshock conditions. To do this, a polynomial was fitted to the 13 computed rates between 5 K and 350 K for each transition and extended to 1400 K. As presented in §4.3 (and figures therein), O_2 is formed in the postshock gas downstream of where H_2O and OH are formed. At the postshock distance where the O_2 abundance approaches its peak, gas temperatures have typically dropped below about 500 K. Thus, rates up to 1400 K suffice.

Because O_2 has no dipole moment and can only emit quadrupole radiation, the line center optical depth is small under almost all circumstances. As a result, the emergent line intensity is proportional to the O_2 column density, $N(O_2)$. The range of H_2 densities and O_2 abundances over which the postshock O_2 emission peaks is determined from the postshock densities, temperature, and abundances computed for each shock model, combined with the radiative transfer calculations; however, $N(O_2)$ also depends on the line-of-sight depth of the shock, which is difficult to assess. A study of water maser emission from behind *C*-type shocks by Kaufman & Neufeld (1996b) suggests that the aspect ratio of the zone of H_2O emission – i.e., the ratio of the line-of-sight shock depth to the cross-sectional width of the high- H_2O abundance zone on the plane of sky – could exceed a factor of 100. For our purposes, we assume the shock width (in the plane of the sky) equals the distance between where the postshock gas temperature first rises above 10 K to where it first drops back to 10 K. We then multiply this distance by 100 to obtain the line-of-sight depth of the O_2 emitting gas. However, our analysis is not tied to the H_2 and O_2 column densities thus derived since the total integrated intensity measured for each O_2 line depends not only on $N(O_2)$, but also on the number of shocked regions within the *Herschel*/HIFI beams, and hence the total spatial extent of the O_2 emission within these beams. The spatial extent of the O_2 emission was only weakly constrained by Chen et al. (2014), other than inferring that the O_2 emission most likely did not fill the *Herschel*/HIFI beams at 487, 774, and 1121 GHz. Thus, we treat the spatial extent of the O_2 emission as a free parameter.

We seek to match *both* the absolute O_2 line fluxes and the observed line ratios. We first derive the column densities and emission area needed to reproduce the measured O_2 487 GHz line flux. The ratio of the accompanying line fluxes at 774 GHz and 1121 GHz to that at 487 GHz are then compared with those observed. We assume that the H_2 and O_2 column densities and emission area needed to reproduce the observed 487 GHz O_2 line flux are given by:

$$N(\text{H}_2) = 100 \times n(\text{H}_2) d_{10} \gamma \quad (1)$$

$$N(\text{O}_2) = N(\text{H}_2) \chi(\text{O}_2) , \quad (2)$$

where 100 is the assumed aspect ratio, $n(\text{H}_2)$ is the H_2 postshock density in the zones where 487 GHz emission peaks, d_{10} is the postshock distance between where the gas temperature first rises above 10 K and where it first returns to 10 K, and $\chi(\text{O}_2)$ is the O_2 abundance relative to H_2 . Because the O_2 column density required to reproduce the observed optically thin line flux is inversely proportional to the area of the emitting region, we introduce the scaling factor γ , which is defined as

$$\gamma = \frac{400 \text{ sq. arcsec}}{A_{487}} , \quad (3)$$

where 400 sq. arcsec is chosen to be roughly consistent with the area of the O_2 emitting region assumed by Chen et al. (2014), and A_{487} is the actual area of the O_2 487 GHz emission in sq. arcsec were it known. Since we compute the 487, 774, and 1121 GHz line emission as a function of postshock depth, the area of the 774 GHz and 1121 GHz emitting regions, relative to A_{487} , is computed for each shock model and scale as

$$\text{Relative area of 774 GHz emitting region} = A_{487} \left(\frac{w_{774}}{w_{487}} \right) \quad (4)$$

$$\text{Relative area of 1121 GHz emitting region} = A_{487} \left(\frac{w_{1121}}{w_{487}} \right) \quad (5)$$

where w_{487} , w_{774} , w_{1121} are the widths of the 487 GHz, 774 GHz, and 1121 GHz emitting regions behind the shock front, respectively. The width of the emitting region in each line is taken to be

the range of postshock depths over which the line flux remains greater than 1 percent of its peak value.

Finally, we define a ‘Goodness of Line Ratio Fit’ parameter to measure how closely each model comes to reproducing the observed 774 GHz and 1121 GHz line fluxes once the 487 GHz line flux has been matched:

$$\text{Goodness of Line Ratio Fit} = \left| \frac{R_{774\text{m}} - R_{774\text{o}}}{R_{774\text{o}}} \right| + \left| \frac{R_{1121\text{m}} - R_{1121\text{o}}}{R_{1121\text{o}}} \right| \quad (6)$$

where $R_{774\text{m}}$ is the model-predicted ratio of the 774 GHz integrated intensity to the 487 GHz integrated intensity, and $R_{774\text{o}}$ is the observed ratio of the 774 GHz integrated intensity to the 487 GHz integrated intensity. Likewise, $R_{1121\text{m}}$ is the model-predicted ratio of the 1121 GHz integrated intensity to the 487 GHz integrated intensity, and $R_{1121\text{o}}$ is the observed ratio of the 1121 GHz integrated intensity to the 487 GHz integrated intensity. Chen et al. (2014) report an observed 487 : 774 : 1121 GHz integrated line intensity ratio of 1 : 1.90 : 0.53 toward Orion H₂ Peak 1. As indicated by Eqn. (6), model-predicted line ratios that exactly match the observed ratios would result in a ‘Goodness of Line Ratio Fit’ of zero.

4.3. Shock Models Results

The results for shock models of varying preshock density, shock velocity and FUV field, computed for $G_o = 0.1, 1, \text{ and } 10$, are shown in Figs. 5, 6, 7, respectively. Only those models that produce a ‘Goodness of Line Ratio Fit’ less than 6 for $G_o = 0.1$ and 1, and less than 14 for $G_o = 10$, are shown for clarity. The best-fit model for each value of G_o is summarized in Table 2; the O₂ line ratios produced by these best-fit models are shown in Fig. 8. The profiles of postshock O₂ line integrated intensity, abundance, and temperature for the best-fit $G_o = 0.1, 1, \text{ and } 10$ shocks models are shown in Figs. 9, 10, and 11, respectively. Finally, the line center

optical depth, τ , in the 487, 774, and 1121 GHz transitions was evaluated for each of the best-fit results given in Table 2. In no case did τ exceed 0.07 and, in most cases, was significantly lower, thus justifying the optically thin assumptions made here.

5. DISCUSSION

Following more than six years of observations, and more than 7000 Galactic lines of sight surveyed, the *SWAS* mission reported only one tentative detection of O₂, toward the Rho Ophiuchi molecular cloud (Goldsmith et al. 2002). Likewise, the *Odin* mission reported only upper limits to the O₂ line strengths (Pagani et al. 2003; Sandqvist et al. 2008), with the exception of one possible detection, also toward the Rho Ophiuchi cloud (Larsson et al. 2007). The upper limits to the O₂ abundance set by *SWAS* and *Odin* are more than 100 times lower than that predicted by equilibrium gas-phase chemical models. This discrepancy was later understood to be primarily the result of the exclusion of dust grains from these models, which serve as important sites for both the freeze out of H₂O and the surface formation of H₂O. This water ice subsequently remains locked on grain surfaces until either photodesorbed by FUV or X-ray photons, sublimated at grain temperatures above ~ 100 K, or sputtered by shocks with velocities $\gtrsim 25$ km s⁻¹ (Draine et al. 1983; Neufeld et al. 2014). By sequestering large amounts of elemental oxygen in water ice, Bergin et al. (2000) and Hollenbach et al. (2009) showed that the gas-phase production of O₂ is effectively suppressed.

The *Herschel* Oxygen Project, guided by these updated models, used *Herschel*'s greater sensitivity to continue the search for O₂. To date, however, Rho Ophiuchi (Liseau et al. 2012) and Orion H₂ Peak 1 remain the only sources with statistically significant O₂ detections. It might be expected that processes common to both sources, yet rare overall, could account for the O₂ emission. Unfortunately, the conditions inferred by Liseau et al. to explain the O₂ emission toward Rho Ophiuchi are insufficient to account for the emission toward Orion H₂ Peak 1. In particular,

toward Rho Ophiuchi, the O₂ emission is attributed to a combination of two emitting regions, one with $N(\text{O}_2) > 6 \times 10^{15} \text{ cm}^{-3}$ and $T < 30 \text{ K}$, and the other with $N(\text{O}_2) = 5.5 \times 10^{15} \text{ cm}^{-3}$ and $T > 50 \text{ K}$. The inferred beam-averaged O₂ abundance is $\sim 5 \times 10^{-8}$ in the warmer component, and somewhat higher in the colder component. The successful detection of O₂ toward this source, among the many sources toward which no O₂ emission was detected, was attributed to time-dependent quiescent cloud chemistry – i.e., Rho Ophiuchi was surmised to have been observed during a relatively short period when the evolving O₂ abundance was near its peak.

Such a scenario is unlikely to apply to Orion H₂ Peak 1. First, the constraints on the spatial extent of the O₂ emission toward Peak 1 provided in Chen et al. (2014) – i.e., an O₂ emitting region less than 25'' in diameter – require that the O₂ column density be between about $3 \times 10^{17} \text{ cm}^{-2}$ and $3 \times 10^{18} \text{ cm}^{-2}$ to produce the absolute O₂ line intensities measured. O₂ column densities this high are hard to produce in quiescent gas (e.g., Hollenbach et al. 2009). Second, Peak 1 is the site of intense shock, rather than quiescent cloud, emission. Third, *if* a component of quiescent gas close to H₂ Peak 1 were responsible for the O₂ emission, and the O₂ abundance were close to its quiescent cloud peak of $\sim 5 \times 10^{-8}$, as in Rho Ophiuchi, the required H₂ column density, $N(\text{H}_2) = N(\text{O}_2) / \chi(\text{O}_2)$, would be on the order of 10^{25} cm^{-2} , which is much higher than observed. Thus, process(es) different from those invoked to explain the O₂ emission toward Rho Ophiuchi are needed to explain the detections toward Orion H₂ Peak 1.

In addition to the presence of shock activity, Orion is the site of O and B stars that produce strong FUV radiation. The FUV field near the Trapezium has been estimated to be $G_o \gtrsim 10^4$ based upon the total radiation from the Trapezium stars – and the O star θ^1 Ori C in particular. The intensity of this field is corroborated by the strength of the far-infrared [C II] and [O I] fine-structure lines mapped toward the Orion molecular ridge, the strength of several near-infrared lines whose intensities have been ascribed to recombinations to highly excited states of CI, and the strength of near-infrared NI lines excited by the fluorescence of UV lines (Herrmann

et al. 1997; Marconi et al. 1998; Walmsley et al. 2000). The amount by which the FUV field is attenuated between the Trapezium and H₂ Peak 1 due to intervening material is uncertain, as is the FUV radiation from other B stars in the Orion cloud. However, as discussed in §3, even modest amounts of FUV radiation (i.e., $G_o \leq 10$) can affect both the structure of and chemistry behind *C*-type shocks and motivate the study here.

FUV-illuminated *C*-type shocks provide a natural explanation for the Orion H₂ Peak 1 O₂ emission for three reasons. First, as discussed in §3.2 and §3.3, the FUV field can increase the atomic oxygen abundance in the preshock gas, which will increase the peak H₂O abundance in the postshock gas. Second, the postshock OH abundance (and, ultimately, the O₂ abundance) is increased via the photodissociation of H₂O as well as OH-producing chemical reactions, some with high activation barriers, enabled by the elevated postshock gas temperatures. By raising the O₂ abundance above that attainable in cold quiescent gas, the implied H₂ column density can be brought closer to observed values. Finally, the similarity between the LSR velocities measured for the O₂ lines of $\approx 11 \text{ km s}^{-1}$ (see Chen et al.), and those measured for the 22 GHz and 621 GHz H₂O masers of $10\text{--}13 \text{ km s}^{-1}$, suggests a possible physical connection. As discussed in §4.1, the maser emission indicates that some shocks are propagating in the plane of the sky, which can potentially provide a higher line-of-sight column density of O₂ than face-on shocks while allowing for the narrow observed O₂ line widths.

For these reasons, as well as the conspicuous presence of shock activity associated with H₂ Peak 1, both Chen et al. (2014) and we focus on shocks as the most likely source of the detected O₂ emission. However, three significant differences distinguish the approach previously taken by Chen et al. and that taken here. First, Chen et al. assume that the preshock gas and the shock are fully shielded from FUV radiation, with only the postshock gas subject to a FUV field. Here, we assume that the preshock, shock, and postshock gas are illuminated by a common FUV field. Given that the width of the shock front is approximately 10^{16} cm or less (see Figs. 9, 10, and

11), this approach seems well justified. In particular, the analysis presented here avoids the inconsistency in which the postshock physical conditions are determined assuming the absence of FUV radiation while the postshock chemistry, which is governed by these physical conditions (e.g., density and temperature), requires the presence of FUV radiation.

Second, the above is important since the effects of FUV radiation on the shock structure can result in substantial changes to the shock width and postshock temperature, with the latter affecting the postshock chemistry. As shown in Fig. 2, for a given preshock density and shock velocity, increasing the FUV field intensity both increases the peak postshock temperature and reduces the shock width. As shown in Bergin et al. (1998), the formation rate of H₂O via the neutral-neutral reactions $O+H_2 \rightarrow OH+H$; $OH+H_2 \rightarrow H_2O+H$ becomes important when the postshock temperature exceeds ~ 300 K and increases rapidly with temperature. In fact, as the peak postshock temperature rises with increasing G_o , the H₂O formation rate begins to exceed the H₂O photodestruction rate resulting in a net increase in the postshock H₂O abundance with G_o (e.g., compare Fig. 2 middle and bottom panels). This trend continues up to the full conversion into H₂O of all gas-phase O nuclei not locked in CO. Only when the postshock cooling causes the temperature to drop below about 300 K does the H₂O formation rate decrease significantly. When this occurs, photodestruction dominates formation and the H₂O abundance begins to decline, as shown in Fig. 2. Ignoring the effects of FUV radiation leads to an underestimate of the postshock temperature and the postshock depth to which H₂O exists in high abundance as well as an overestimate of the shock width, all of which affect the resulting O₂ emission.

Third, since O₂ is formed from the photo-destroyed products of H₂O, i.e., O and OH, H₂O must be relatively abundant (i.e., $\chi(H_2O) > 10^{-5}$) in the postshock gas to produce the observed O₂ emission. There are two ways to achieve this: (1) by placing H₂O into the gas phase directly through the sputtering of H₂O from the ice-covered mantles of dust grains behind the shock; and, (2) by chemically forming H₂O behind the shock via the neutral-neutral reactions above.

However, for process (2) to form a high H₂O abundance, the preshock gas must have a high abundance of atomic oxygen. Within gas in which the H₂O depletion onto grains is significant, Chen et al. require that the sputtering efficiency be $\gtrsim 10\%$ behind a 12 km s⁻¹ shock. This efficiency exceeds all theoretical predictions of which we are aware, including Draine et al. (1983), Jiménez-Serra et al. (2008, see their Figure 7), and Flower & Pineau des Florêts (2010). Recently, Neufeld et al. (2014) have modeled the water abundance behind interstellar shocks based on *Herschel* measurements of far-infrared (IR) and submillimeter measurements of CO and H₂O in combination with *Spitzer* measurements of mid-IR H₂ rotational emission. Their best-fit results are in good agreement with the prediction that only when shocks reach a velocity of $\gtrsim 25$ km s⁻¹ will H₂O be completely removed from grain mantles. Thus, it is not clear that sufficient H₂O can be removed from grain mantles to support the model offered in Chen et al. if depletion of H₂O onto dust grains is significant in the preshock gas and negligible sputtering efficiency is assumed behind a 12 km s⁻¹ shock.

Alternately, Chen et al. suggest that the preshock gas is sufficiently young that depletion is minimal, in which case the atomic oxygen abundance is high. However, since this model assumes the preshock gas is collapsing from an initial density of 100 cm⁻³, the time between when the density evolves to its required preshock value (i.e., 4.2×10^4 cm⁻³) and when depletion becomes important is $\sim 1.7 \times 10^6$ years. Nevertheless, invoking a short interval during which the preshock is sufficiently dense, but undepleted, could result in the high preshock O abundance needed to yield a postshock H₂O abundance sufficient to produce detectable O₂ emission. A short-lived period in which both the preshock gas density and O abundance are high could also account for the rarity of O₂ detections, as discussed by Chen et al. However, this model still presumes the preshock gas is fully shielded while the postshock gas is not, an assumption not justified in the Chen et al. model.

Introducing a FUV field to the preshock gas solves these problems. FUV photons can photodes-

orb H₂O from grain mantles when shock velocities are too low to produce significant sputtering (i.e., $v_s \lesssim 20 \text{ km s}^{-1}$). (When shock velocities are $\gtrsim 25 \text{ km s}^{-1}$, sputtering will remove any H₂O not photodesorbed in the preshock gas.) Even if the FUV field results in the photodestruction of gas-phase H₂O in the preshock gas, the O and OH produced will be rapidly converted to H₂O in the warm postshock gas. Thus, a FUV field can eliminate the need for high assumed sputtering efficiencies at low shock velocities while relaxing the need to invoke a particular epoch in the time-dependent evolution of the preshock gas. As for time-dependent preshock evolution being the cause for the rarity of O₂ detections, a different explanation is suggested below.

Table 2 lists shock models considered here that both reproduce the absolute O₂ line intensities and line ratios for incident FUV fields having a $G_o = 0.1, 1, \text{ and } 10$. Several trends are evident. First, as discussed in §3, as G_o increases, the ion-neutral coupling increases and the width of the shock decreases. This is evident in the scale of the x -axes in Figs. 2, 9, 10, 11. Likewise, as G_o increases, roughly the same postshock temperatures are achieved with decreasing shock velocities. Second, as G_o increases, the increased photodissociation of molecules lowers the peak postshock abundance of H₂O, OH, and O₂, thus requiring greater H₂ column densities to produce the same optically-thin O₂ line flux (see Table 2).

Within the observational uncertainties, all three models in Table 2 can explain both the measured O₂ line fluxes and line ratios; is one model preferred? One possible discriminator is the degree to which each model agrees with estimates of the total H₂ column density and number density toward Peak 1. Rosenthal, Bertoldi & Drapatz (2000) estimate the H₂ column density to be $\approx 2 \times 10^{22} \text{ cm}^{-2}$ based on the observation of 56 H₂ ro-vibrational and pure rotational lines toward Peak 1 using the *Infrared Space Observatory's* Short Wavelength Spectrometer (de Graauw et al. 1996). However, because the lowest-lying H₂ pure rotational transition lies 510 K above the ground state, estimates based on H₂ lines are more sensitive to the warm and hot gas and much less so to the cooler (i.e., $T < 100 \text{ K}$) gas where the O₂ emission peaks.

The cooler gas is better, if less directly, sampled by ^{12}CO and its isotopologues. Using multi-line transitions of ^{12}CO , ^{13}CO , and C^{18}O , Peng et al. (2012) derive a ^{12}CO column density of between $5 \times 10^{18} \text{ cm}^{-2}$ and 10^{19} cm^{-2} toward Peak 1, in good agreement with earlier estimates of González-Alfonso et al. (2002). This corresponds to an H_2 column density of between $6 \times 10^{22} \text{ cm}^{-2}$ and $1.2 \times 10^{23} \text{ cm}^{-2}$, assuming a ^{12}CO abundance of 8×10^{-5} (Wilson & Matteucci 1992). However, even these studies rely on transitions with upper level temperatures above the ground state $> 32 \text{ K}$ and may exclude contributions from a colder component.

Estimates of the preshock H_2 number density vary depending on the tracer being modeled. Generally, estimates exceed 10^5 cm^{-3} , and can range as high as 10^8 cm^{-3} (cf. Kaufman & Neufeld 1996a; Rosenthal, Bertoldi & Drapatz 2000; González-Alfonso et al. 2002). None of the models we are aware of suggest that preshock densities toward Peak 1 are less than 10^4 cm^{-3} .

While none of the models we considered is in perfect agreement with the Peak 1 H_2 column density and number density estimates, the best-fit model in Table 2 that assumes $G_o = 1$ comes closest. Moreover, the shock velocity of this model (i.e., 23 km s^{-1}) is within the range of typical shock speeds in OMC-1 of $30 \pm 10 \text{ km s}^{-1}$ (Kristensen et al. 2003, 2007).

The best-fit $G_o = 0.1$ model is a good approximation to the fully-shielded C -type shock models that have traditionally been used to model a wide variety of molecular emission toward outflows. We show that fully-shielded (i.e., $G_o \leq 0.1$) models fail to reproduce the O_2 line intensities and ratios with shock conditions inferred from other data; however, allowing for the presence of even modest amounts of FUV radiation (i.e., $G_o \gtrsim 1$) provides a better fit to the observations.

Finally, we note that the circumstances that explain the O_2 emission toward Orion H_2 Peak 1 may also explain the rarity of similar detections in other sources. First, the shocked gas emission around Peak 1 subtends $\sim 20''$, larger than for most outflows. Since the strength of the optically-thin line emission within the beam scales with the O_2 column density \times the area of the emitting region, the column density requirements are eased if the emitting area is large, as toward Peak

1. Second, the presence of strong H₂O maser emission toward the position of the O₂ detections is evidence not only for the presence of shocks, but for some shocks propagating in the plane of the sky. High postshock temperatures promote the production of O₂ well above abundance levels predicted for cold quiescent gas, while the geometry (in the plane of the sky) provides the observer with a potentially large line-of-sight column of gas with this relatively high O₂ abundance. Of course, shocks of the sort described here would be expected to produce enhanced optically thin O₂ emission regardless of whether these shocks were propagating perpendicular to our line of sight or not. However, if such shocks produce O₂ integrated intensities comparable to what was detected toward Peak 1, but with propagation angles closer to our line of sight, the O₂ line profiles would appear broader. Thus, the same total line flux would be spread over a greater number of velocity bins with a corresponding reduction in the line center amplitude. For weak emission, such as that exhibited by the observed O₂ lines, narrow lines are generally much easier to detect than lower amplitude broad lines, particularly in the presence of noise. The rarity of O₂ detections may therefore result from the need to simultaneously satisfy four conditions: (1) an O₂ emitting area that fills a non-negligible fraction of a beam; (2) the presence of *C*-type shocks having peak postshock temperatures sufficient to drive the efficient production of H₂O; (3) illumination by FUV radiation that can both enhance the preshock gas-phase O-nuclei abundance and photodissociate postshock H₂O; and, (4) a shock propagation vector close to perpendicular to the line of sight that naturally provides narrow line profiles.

We wish to acknowledge helpful discussions with Paul Goldsmith. This work was supported by NASA through Astrophysics Data Analysis Program grant No. NNX13AF16G.

REFERENCES

- Beckwith, S., Persson, S.E., Neugebauer, G., & Becklin, E.E. 1978, ApJ, 223, 464
- Bergin, E. A., Melnick, G. J., & Neufeld, D. A. 1998, ApJ, 499, 777
- Bergin, E. A., Melnick, G. J., Stauffer, J. R. et al. 2000, ApJ, 539, L129
- Chen, J-H., Goldsmith, P. F., Viti, S., et al. 2014, to appear in ApJ
- Cunningham, N. J. 2006, PhD Thesis, University of Colorado
- de Graauw Th., Haser L., Beintema D., et al. 1996, A&A, 315, L49
- de Graauw, Th., Helmich, F. P., Phillips, T. G., et al. 2010, A&A, 518, L6
- Draine, B.T. 1983, ApJ, 270, 519
- Draine, B.T., Roberge, W.G., & Dalgarno, A. 1983, ApJ, 264, 485
- Flower, D. R., & Pineau des Florêts, G. 1994, MNRAS, 268, 724
- Flower, D. R., & Pineau des Florêts, G. 2010, MNRAS, 406, 1745
- Gautier, T.N., III, Fink, U., Treffers, R.P., & Larson, H.P. 1976, ApJL, 207, L129
- Genzel, R., Reid, M. J., Moran, J. M., & Downes, D. 1981, ApJS, 30, 145
- Goldsmith, P. F., & Langer, W. D. 1978, ApJ, 222, 881
- Goldsmith, P. F., Li, D., Bergin, E. A., et al. 2002, ApJ, 576, 814
- Goldsmith, P. F., Liseau, R., Bell, T. A., et al. 2011, ApJ, 737, 96
- Goldsmith, P. F., Melnick, G.J., Bergin, E.A., et al. 2000, ApJL, 539, L123

- Goldsmith, P. F., Snell, R. L., Erickson, N. R., et al. 1985, *ApJ*, 289, 613
- González-Alfonso, E., Wright, C. M., Cernicharo, J., et al. 2002, *A&A*, 386, 1074
- Habing, H. J. 1968, *Bull. Astron. Inst. Netherlands*, 19, 421
- Herrmann, F., Madden, S. D., Nikola, T., et al. 1997, *ApJ*, 481, 343
- Hollenbach, D.J., Kaufman, M. J., Bergin, E.A., & Melnick, G.J. 2009, *ApJ*, 690, 1497
- Jiménez-Serra, I., Caselli, P., Martín-Pintado, M., et al. 2008, *A&A*, 482, 549
- Kaufman, M. J. & Neufeld, D. A. 1996a, *ApJ*, 456, 611
- Kaufman, M. J. & Neufeld, D. A. 1996b, *ApJ*, 456, 250
- Kristensen, L. E., Gustafsson, M., Field, D., et al. 2003, *A&A*, 412, 727
- Kristensen, L. E., Ravkilde, T. L., Field, D., et al. 2007, *A&A*, 469, 561
- Kristensen, L. E., van Dishoeck, E. F., Bergin, E. A., et al. 2012, *A&A*, 542, A8
- Larsson B., Liseau R., Pagani L., et al. 2007, *A&A*, 466, 999
- Lique, F. 2010, *J. Chem. Phys.*, 132, 044311
- Liseau, R., Goldsmith, P. F., Larsson, B., et al. 2012, *A&A*, 541, A73
- Marconi, A., Testi, L., Natta, A., & Walmsley, C. M. 1998, *A&A*, 330, 696
- McElroy, D., Walsh, C., Markwick, A. J., et al. 2013, *A&A*, 550, A36
- Melnick, G. J., Stauffer, J. R., Ashby, M. L. N., et al. 2000, *ApJ*, 539, L77
- Melnick, G. J., Tolls, V., Goldsmith, P. F., et al. 2012, *ApJ*, 752, 26

- Neufeld, D. A., Gusdorf, A., Güsten, R., et al. 2014, *ApJ*, 781, 102
- Neufeld, D.A., Lepp, S. & Melnick, G. J. 1995, *ApJS*, 100, 132
- Neufeld, D. A., & Melnick, G. J. 1991, *ApJ*, 368, 215
- Neufeld, D. A., Wu, Y., Kraus, A., et al. 2013, *ApJ*, 769, 48
- Nordh, H. L., von Schéele, F., Frisk, U., et al. 2003, *A&A*, 402, L21
- Pagani L., Olofsson A. O. H., Bergman P., et al. 2003, *A&A*, 402, L 77
- Peng, T.-C., Wyrowski, F., Zapata, L. A., Güsten, R., & Menten, K. M. 2012, *A&A*, 538, A12
- Pilbratt, G. L., Riedinger, J. R., Passvogel, T., et al. 2010, *A&A*, 518, L1
- Roelfsema, P. R., Helmich, F. P., Teyssier, D., et al. 2012, *A&A*, 537, A17
- Rosenthal, D., Bertoldi, F., & Drapatz, S. 2000, *A&A*, 356, 705
- Sandqvist A., Larsson B., Hjalmarsen, Å., et al. 2008, *A&A*, 482, 849
- van Kempen, T. A., Kristensen, L.E., Herczeg, G.J., et al. 2010, *A&A*, 518, 121
- Walmsley, C. M., Natta, A., Oliva, E., & Testi, L. 2000, *A&A*, 364, 301
- Wilson, T. L., & Matteucci, F. 1992, *A&ARv*, 4, 1

TABLE 1. Summary of O₂ Observations Toward Orion H₂ Peak 1

Rest Frequency (GHz)	Transition ($N, J \rightarrow N, J$)	Energy Above Ground State (E_u/k)	Integrated ^a Intensity (K km s ⁻¹)	Line ^a Width (km s ⁻¹)	LSR Velocity (km s ⁻¹)	HIFI Beam ^b Diameter (arcsec)
487.249	3, 3 – 1, 2	26 K	0.081	3.1	10.2	44.7
773.840	5, 4 – 3, 4	61 K	0.154	1.7	11.0	28.2
1120.715	7, 6 – 5, 6	115 K	0.043	0.8	11.0	18.9

^a After Chen et al. (2014); ^b See Roelfsema et al. (2012).

TABLE 2. Best-Fit Shock Models

G_o	Shock		Peak Postshock		Conditions at Peak of the 487, 774, and 1121 GHz Emission				
	Log ₁₀ Preshock H ₂ Density (cm ⁻³)	Shock Velocity (km s ⁻¹)	O ₂ Abundance (rel. to H ₂)	O ₂ Abundance (rel. to H ₂)	Transition (GHz)	$n(\text{H}_2)$ (cm ⁻³)	$N(\text{H}_2)$ (cm ⁻²)	$\chi(\text{O}_2)$ (rel. to H ₂)	Temp. (K)
0.1 ...	3.4	28	6.0×10^{-6}		487	5.0×10^4	$2.1 \times 10^{23} \cdot \gamma$	6.0×10^{-6}	24
					774	4.9×10^4	$2.1 \times 10^{23} \cdot \gamma$	5.1×10^{-6}	34
					1121	4.7×10^4	$2.0 \times 10^{23} \cdot \gamma$	3.3×10^{-6}	51
1 ...	4.9	23	1.7×10^{-6}		487	1.3×10^6	$3.7 \times 10^{23} \cdot \gamma$	1.7×10^{-6}	24
					774	1.3×10^6	$3.6 \times 10^{23} \cdot \gamma$	1.4×10^{-6}	39
					1121	1.2×10^6	$3.5 \times 10^{23} \cdot \gamma$	1.0×10^{-6}	61
10 ...	6.0	14	1.0×10^{-6}		487	9.5×10^6	$6.2 \times 10^{23} \cdot \gamma$	1.0×10^{-6}	26
					774	9.3×10^6	$6.0 \times 10^{23} \cdot \gamma$	9.3×10^{-7}	47
					1121	9.0×10^6	$5.8 \times 10^{23} \cdot \gamma$	7.7×10^{-7}	73

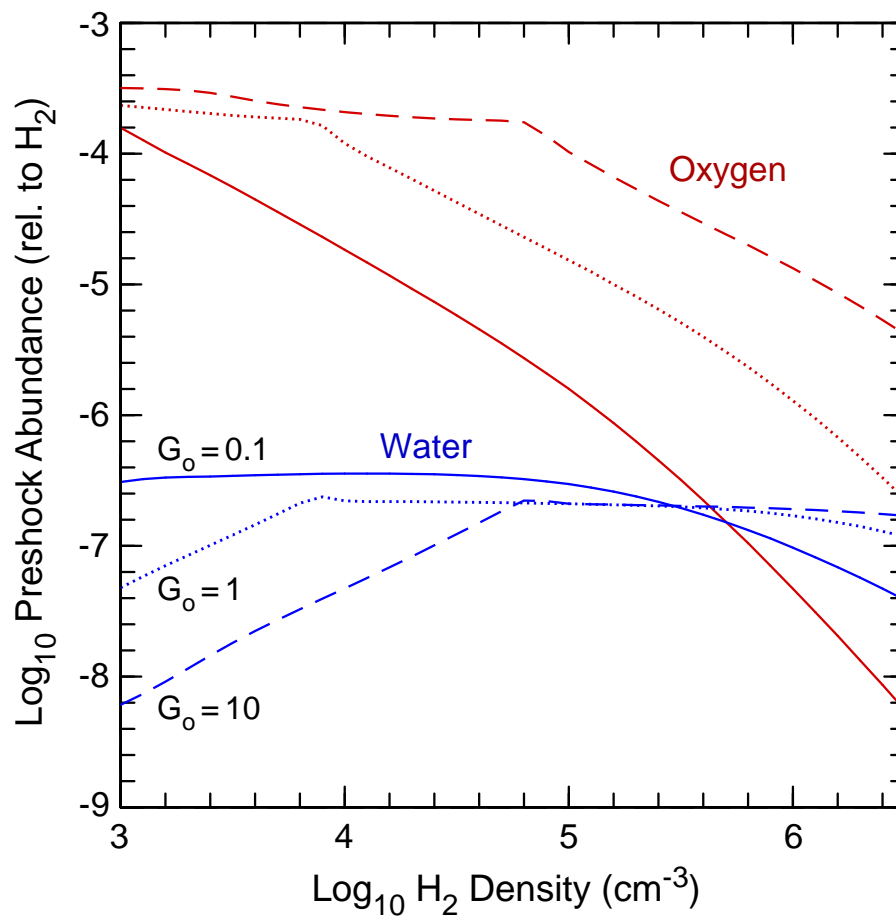


Fig. 1. Preshock gas-phase abundances of atomic oxygen (red curves) and H_2O (blue curves) as a function of preshock H_2 density and FUV field strength, G_o . The abundances are determined from the PDR model used here (see text) assuming a visual extinction $A_V=1.0$ between the FUV source and the preshock gas. For a given density, lower values of G_o result in greater amounts of O incorporated into ice mantles and thus not available in the gas phase. In the absence of sputtering, the preshock gas phase O abundance sets the maximum postshock H_2O abundance.

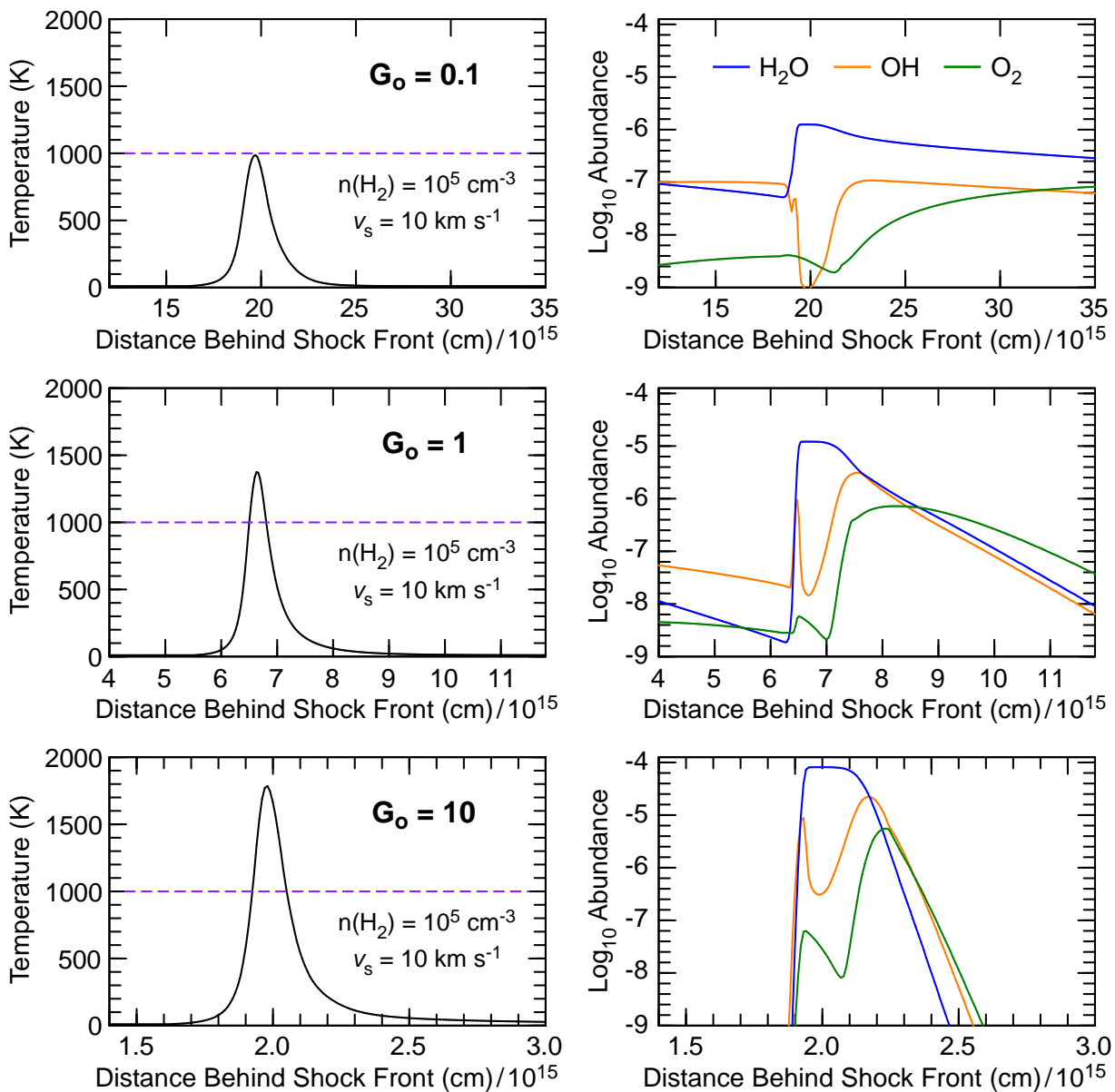


Fig. 2. Profiles of postshock gas temperature (*left panels*) and resulting H₂O, OH, and O₂ abundance (*right panels*) for $G_0 = 0.1$ (*top row*), $G_0 = 1$ (*middle row*), and $G_0 = 10$ (*bottom row*). All models have been run for a preshock H₂ density of 10^5 cm^{-3} and a shock velocity of 10 km s^{-1} . Because this shock velocity is low, the preshock gas-phase O abundance is not increased by sputtering. The fiducial temperature of 1000 K is denoted by a horizontal dashed line in the left panels to highlight the increase in peak postshock temperature with increasing G_0 . Also note that distance behind the shock front at which the gas temperature and H₂O, OH, and O₂ abundances peak, and the length scale over which the elevated temperatures and abundances persist, decrease with increasing G_0 .

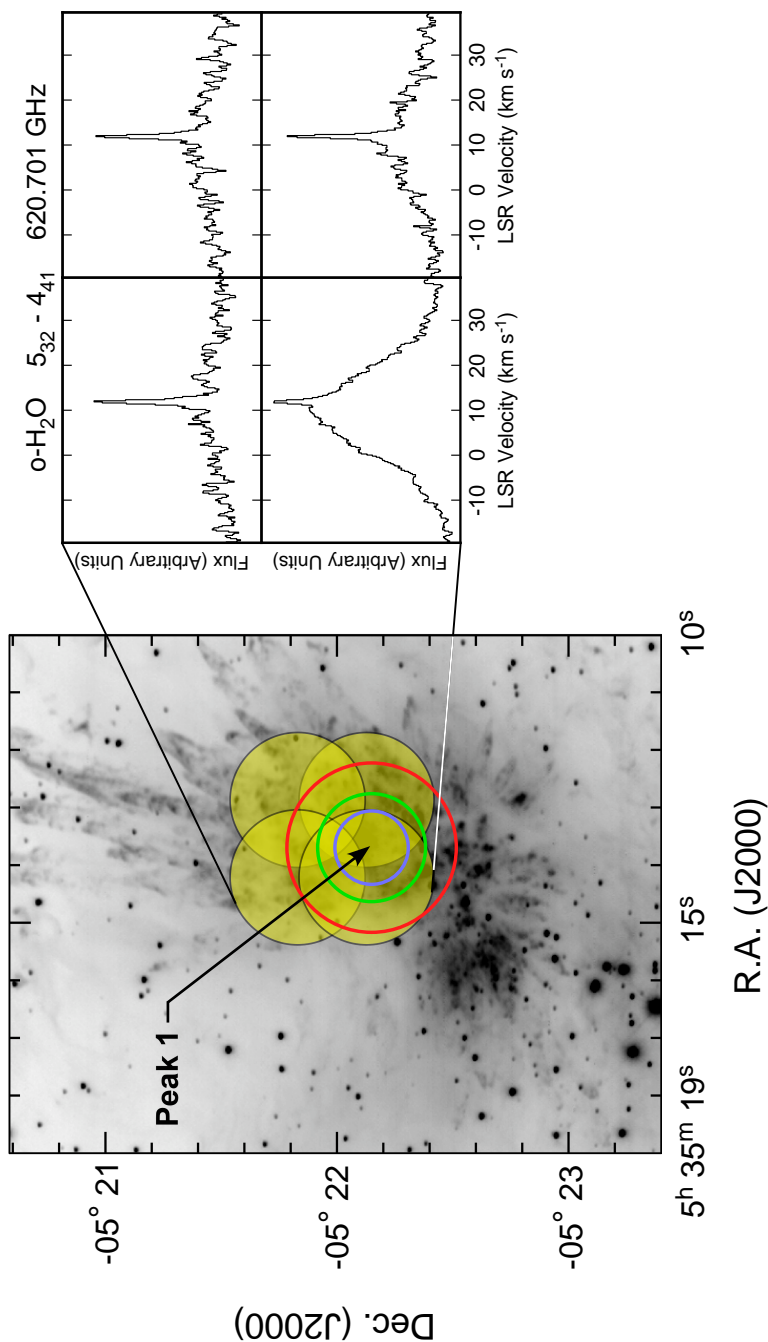


Fig. 3. Position of O₂ 487 GHz (*red circle*), 774 GHz (*green circle*), and 1121 GHz (*blue circle*) beams centered on H₂ Peak 1 ($\alpha_{2000} = 5^{\text{h}} 35^{\text{m}} 13^{\text{s}}.7$, $\delta_{2000} = -5^{\circ} 22' 09''$; after Chen et al. 2014) superposed on the H₂ image obtained by Cunningham (2006). The *Herschel*/HIFI instrument was also used to map a $\sim 2' \times 2'$ region centered on BN/KL; only those positions toward Peak 1 exhibit evidence for H₂O maser emission (Neufeld et al. 2013). The 621 GHz HIFI beams and their sky positions are shown as filled yellow circles. The H₂O spectra, with the prominent maser feature at $\approx 11 \text{ km s}^{-1}$, is shown on the right.

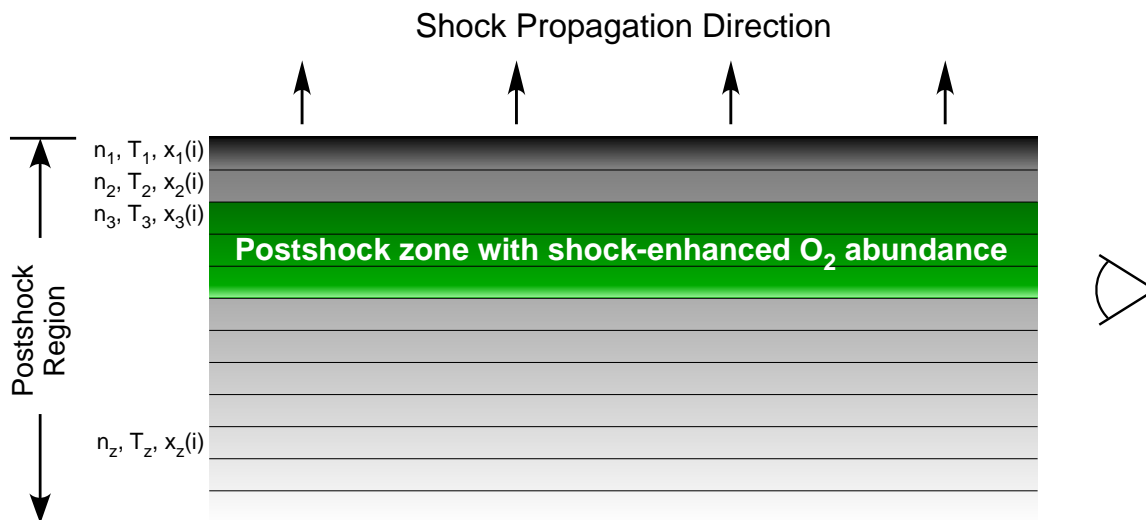


Fig. 4. Proposed scenario in which the O_2 emission arises within gas in which the O_2 abundance is enriched by the passage of a non-dissociative C -type shock. If these shocks are propagating perpendicular to our line of sight, as suggested by the presence of H_2O masers toward Orion H_2 Peak 1, the column density of warm, O_2 -enriched gas can be significantly greater than for face-on shocks. Such a scenario permits a line-of-sight LSR velocity shift of $\sim 12 \text{ km s}^{-1}$, while the perpendicular shock velocity can be a free parameter. Finally, because the line of sight samples gas with a low velocity gradient, consistent with maser production, the measured O_2 line widths of $\leq 3 \text{ km s}^{-1}$ can be understood. The models described here divide the postshock region into 1,000 zones, each of which is characterized by a distinct density, temperature, and set of chemical abundances. The sum of the computed O_2 emission from all of these zones is then compared with the observed integrated intensity in each of the O_2 lines detected.

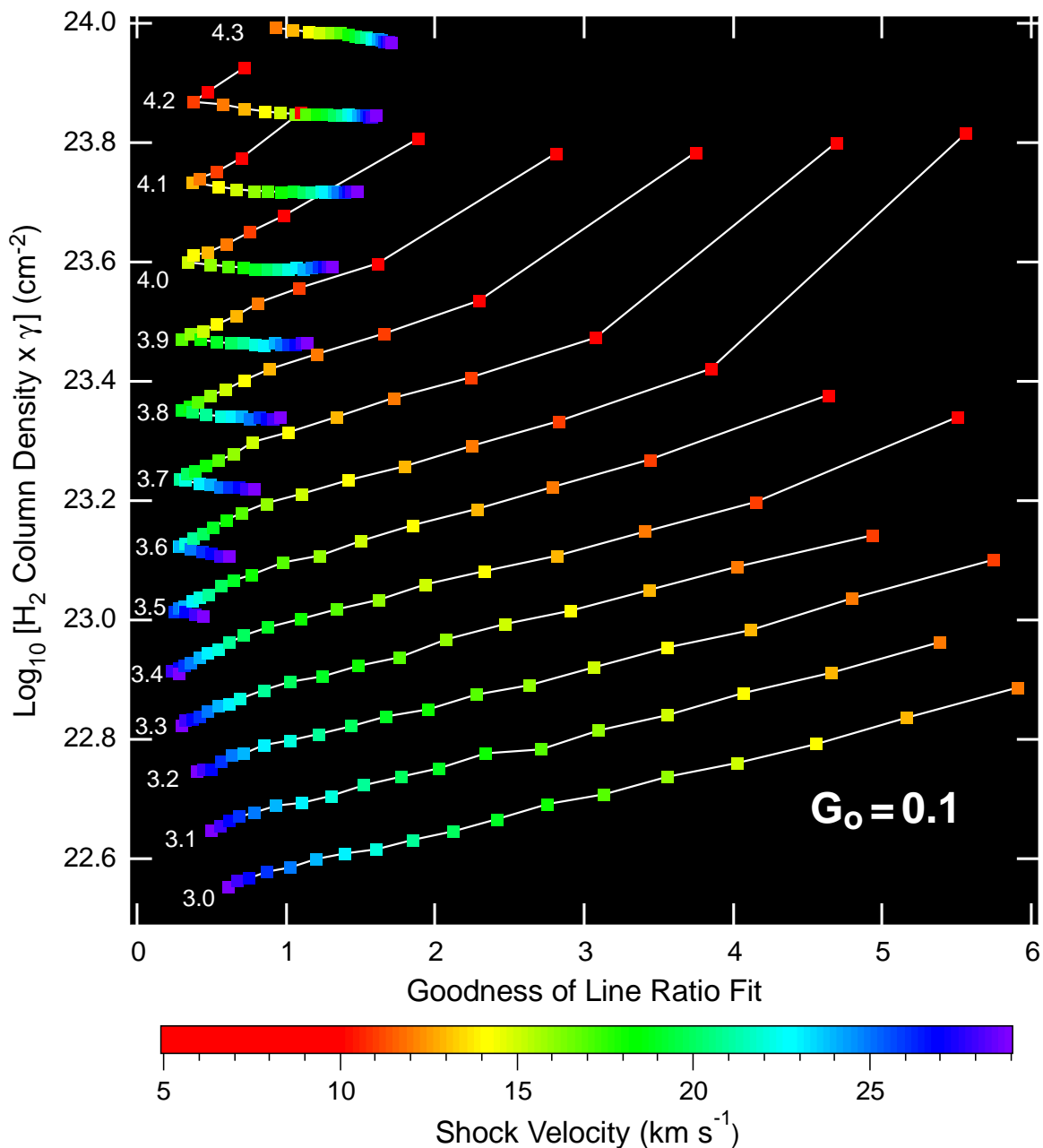


Fig. 5. Plot of the agreement between the predicted and observed 487 GHz, 774 GHz, and 1121 GHz O_2 line ratios produced by various shock models versus H_2 column density and shock velocity for $G_0 = 0.1$. As discussed in the text, the lower the value of the Goodness of Fit, the better the shock conditions reproduce the observed O_2 line ratios, with a value of zero representing a perfect fit. Log_{10} of the preshock H_2 density is shown for each family of models. The required H_2 (and O_2) column density scales inversely with the area of the O_2 emitting region. The above plot assumes a 487 GHz O_2 emitting area of 400 sq. arcseconds (see text).

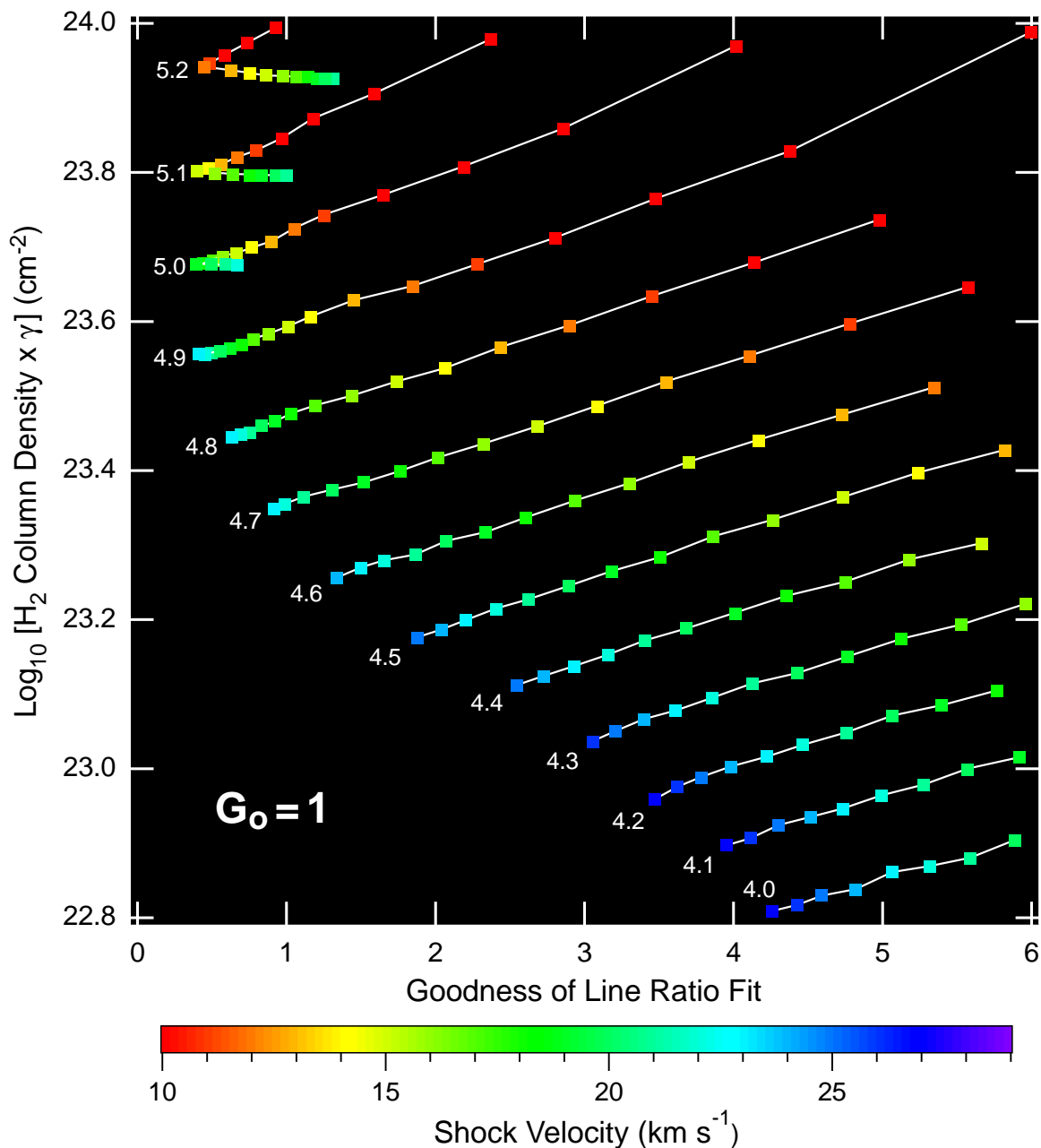


Fig. 6. Plot of the agreement between the predicted and observed 487 GHz, 774 GHz, and 1121 GHz O_2 line ratios produced by various shock models versus H_2 column density and shock velocity for $G_0=1$. As discussed in the text, the lower the value of the Goodness of Fit, the better the shock conditions reproduce the observed O_2 line ratios, with a value of zero representing a perfect fit. Log_{10} of the preshock H_2 density is shown for each family of models. The required H_2 (and O_2) column density scales inversely with the area of the O_2 emitting region. The above plot assumes a 487 GHz O_2 emitting area of 400 sq. arcseconds (see text).

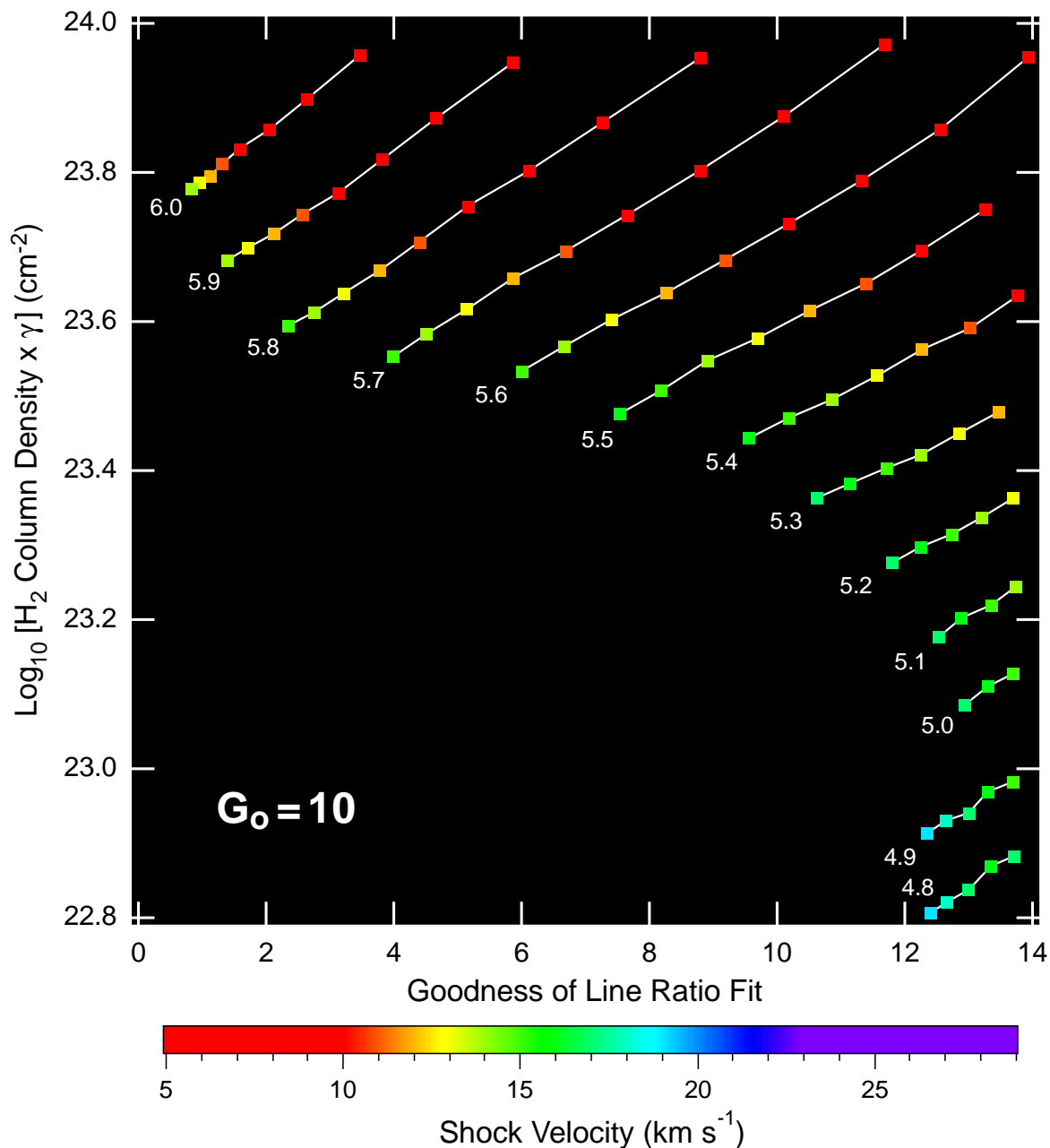


Fig. 7. Plot of the agreement between the predicted and observed 487 GHz, 774 GHz, and 1121 GHz O_2 line ratios produced by various shock models versus H_2 column density and shock velocity for $G_0 = 10$. As discussed in the text, the lower the value of the Goodness of Fit, the better the shock conditions reproduce the observed O_2 line ratios, with a value of zero representing a perfect fit. Log_{10} of the preshock H_2 density is shown for each family of models. The required H_2 (and O_2) column density scales inversely with the area of the O_2 emitting region. The above plot assumes a 487 GHz O_2 emitting area of 400 sq. arcseconds (see text).

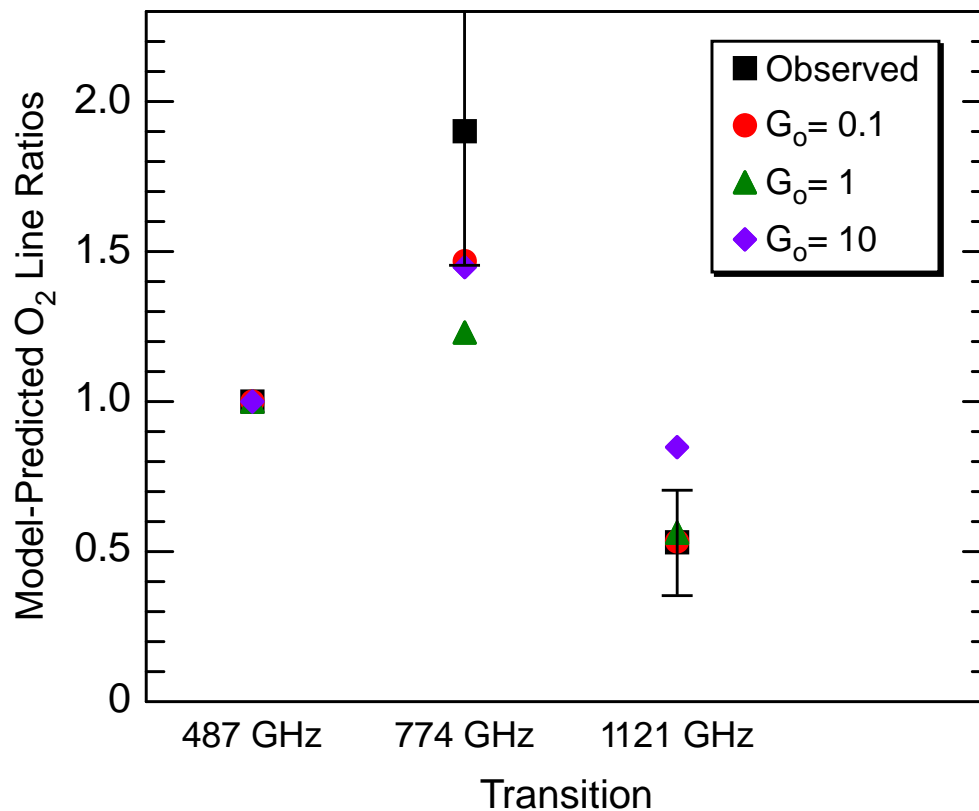


Fig. 8. Ratio of the observed O₂ integrated line intensities to that of the 487 GHz line (*black square*) given by Chen et al. (2014), and those predicted by the best-fit shock model with $G_o = 0.1$ (*red circle*), $G_o = 1$ (*green triangle*), and $G_o = 10$ (*purple diamond*) and detailed in Table 2. As discussed in the text, the shock models have been computed to reproduce the O₂ 487 GHz integrated intensity. The 1σ uncertainties in ratios of the 774 GHz and 1121 GHz line intensities to the 487 GHz line intensity are shown.

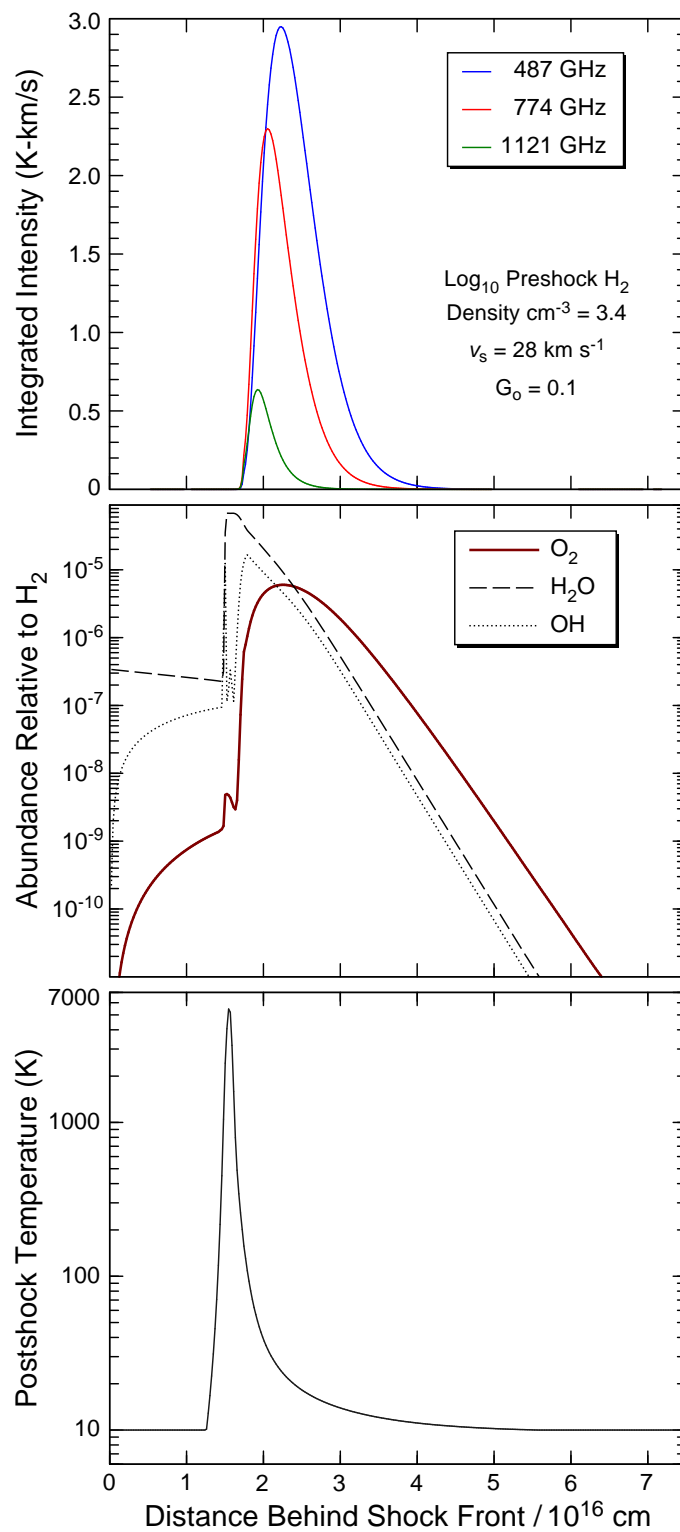


Fig. 9. Profiles of integrated intensity (*top*), abundance (*middle*), and gas temperature (*bottom*) as a function of distance behind the shock front for the best-fit shock parameters for $G_0 = 0.1$.

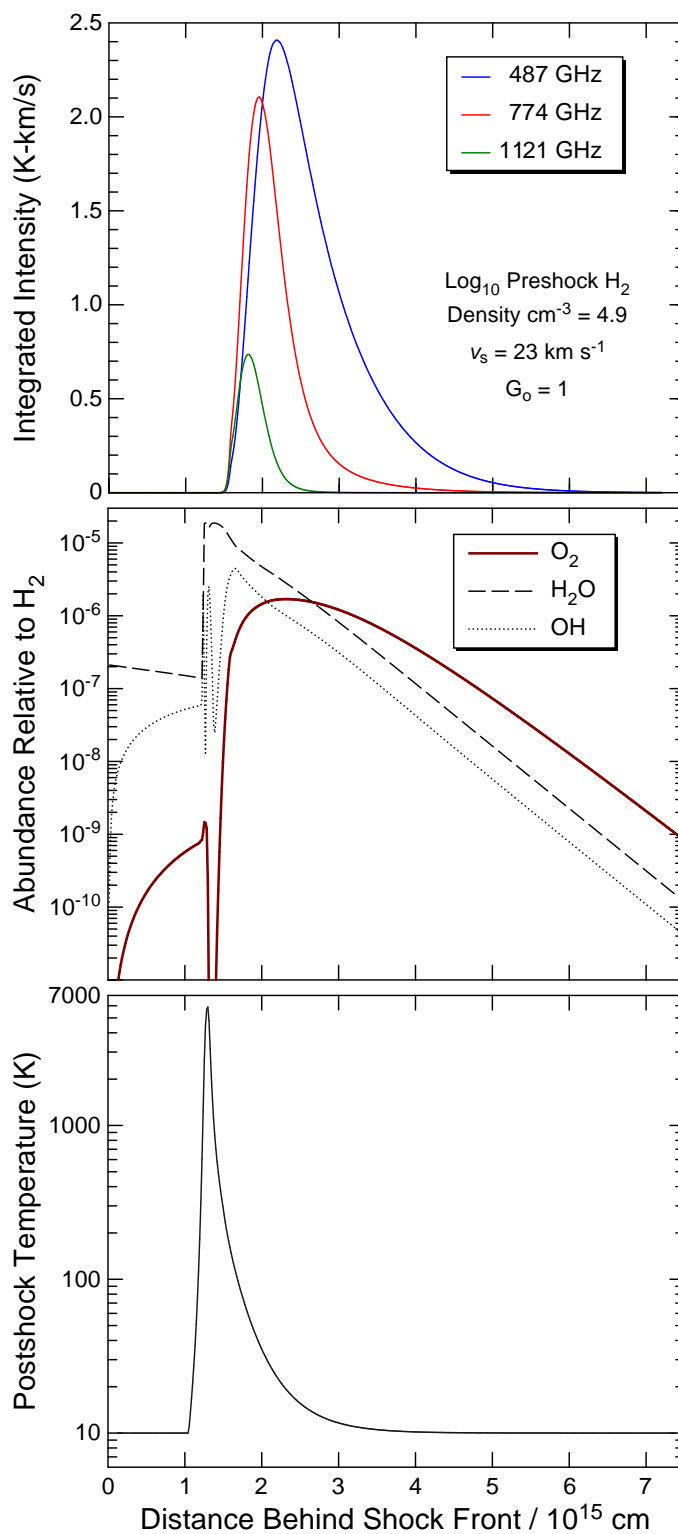


Fig. 10. Profiles of integrated intensity (*top*), abundance (*middle*), and gas temperature (*bottom*) as a function of distance behind the shock front for the best-fit shock parameters for $G_0 = 1$.

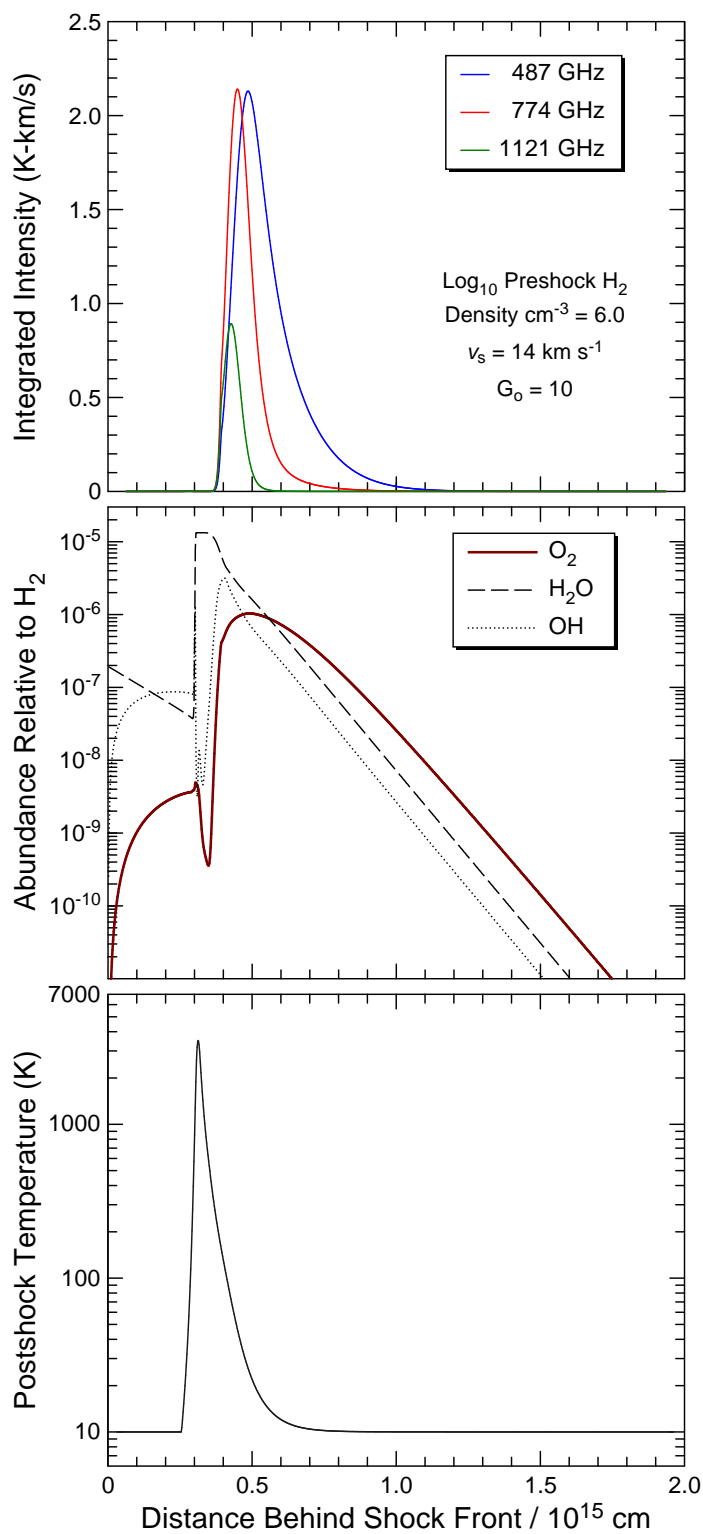


Fig. 11. Profiles of integrated intensity (*top*), abundance (*middle*), and gas temperature (*bottom*) as a function of distance behind the shock front for the best-fit shock parameters for $G_0 = 10$.